AIAA Propulsion and Energy 2019 Forum, 19-22 August 2019, Indianapolis, IN, USA
https://doi.org/10.2514/6.2019-4275

Unsteady Swirl Distortion Characteristics for S-ducts using Lattice Boltzmann and Time-Resolved, Stereo PIV methods

Manuel Guerrero-Hurtado[1], Pavlos K. Zachos[2] David G. MacManus[3] and Matteo Migliorini[4]
Propulsion Engineering Centre, School of Aerospace, Transport and Manufacturing, Cranfield University, Cranfield, MK43 0AL, UK

Giuseppe Trapani[5]
Dassault Systémes España, 28020 Madrid, ES

The unsteady flow fields generated by convoluted aero engine intakes are major sources of instabilities that can compromise the performance of the downstream turbomachinery components. This highlights the need for high spatial and temporal resolution measurements that will allow a greater understanding of the aerodynamics but also improvements in our current predictive capability for such complex flows. This paper presents the validation of a modern Lattice Boltzmann method (LBM) to predict the unsteady flow and swirl distortion characteristics within a representative S-duct intake. The numerical results are compared against high spatial and temporal resolution Particle Image Velocimetry (PIV) data for the same S-duct configuration at an inlet Mach number of 0.27. The work demonstrates that LBM is broadly able to capture the flow topologies and temporal characteristics with the exception of the magnitude of the unsteady fluctuations which were found to be notably under-predicted compared to the PIV data. Proper Orthogonal Decomposition analysis shows that LBM is able to provide the key flow modes and their spectral distributions which were found broadly in alignment with the PIV data. A statistical assessment of the unsteady distortion history highlights that LBM can also provide representative distributions of the main swirl distortion descriptors. Overall the work demonstrates that LBM shows promising potential for S-duct unsteady flow predictions which combined with the minimum computational grid requirements, robustness and fast convergence make it an attractive solution for wider use in the area of unsteady propulsion system aerodynamics.

[1] Researcher, Propulsion Engineering Centre, Cranfield University, M43 0AL, UK.
[2] Lecturer in Aerodynamics, Propulsion Engineering Centre, Cranfield University, M43 0AL, UK, AIAA Member.
[3] Professor of Propulsion Aerodynamics and Installations, Propulsion Engineering Centre, Cranfield University, M43 0AL, UK, AIAA Member.
[4] Doctoral researcher, Propulsion Engineering Centre, Cranfield University, M43 0AL, UK, AIAA Member.
[5] XFlow Application Engineer, Dassault Systémes España, 28020 Madrid, Spain, AIAA Member

Nomenclature

List of symbols

A	=	Area
D	=	Diameter
dt	=	Time step, sec
e_i	=	Discrete velocity direction
$f_i(\mathbf{r},t)$	=	Particle distribution function at time t and position $\mathbf{r}$
h	=	Offset
k	=	Swirl pairs index and total number of modal contributions
L	=	Length
M	=	Mach number
M_{ij}	=	PDFs to moments' transformation matrix
Re_D	=	Diameter based Reynolds number
R	=	AIP radius, m
r	=	AIP radial position, mm
$\mathbf{r}$	=	Position vector in the x,y,z space
St	=	Strouhal number
$SS^{+}_{i,k}$	=	Positive Sector Swirl in the k-th swirling region of the i-th ring
$SS^{-}_{i,k}$	=	Negative Sector Swirl in the k-th swirling region of the i-th ring
u, v, w	=	Velocity vector cartesian components, m/s
V_{ip}	=	In-plane velocity, m/s
$y+$	=	Non-dimensional distance from the wall
ν_t	=	Turbulent Eddy Viscosity
x, y, z	=	Cartesian system of reference coordinates

Abbreviations

AIP	=	Aerodynamic Interface Plane
CDI	=	Circumferential Distortion Index
CFD	=	Computation Fluid Dynamics
DC(θ)	=	Distortion coefficient for a sector of θ deg.
(D)DES	=	(Delayed) Detached Eddy Simulation
DEHS	=	Di-Ethyl-Hexyl Sebacate
FSM	=	First Switching Mode
FVM	=	First Vertical Mode
j-PDF	=	Joint Probability Distribution Function
LBM	=	Lattice Boltzmann Method
LES	=	Large Eddy Simulation
MRT	=	Multiple Relaxation Time
PAW	=	Propulsion Aerodynamics Workshop
POD	=	Proper Orthogonal Decomposition
PDF	=	Probability Density Function
PS	=	Power Spectrum
RDI	=	Radial Distortion Index
SAE	=	Society of Automotive Engineering
SD	=	Swirl Directivity
SI	=	Swirl Intensity
SP	=	Swirl Pairs
SRT	=	Single Relaxation Time
SSM	=	Second Switching Mode
SVM	=	Second Vertical Mode
TKE	=	Turbulent Kinetic Energy
TR-PIV	=	Time Resolved Particle Image Velocimetry
(U)RANS	=	(Unsteady) Reynolds Averaged Navier Stokes
WALE	=	Wall-Adapting Local Eddy Viscosity

Subscripts

i	=	Index *i*
in	=	Inlet plane
k	=	Index *k*
l	=	Index *l*
m	=	Index *m*
max	=	Maximum
min	=	Minimum
out	=	Exit plane
ref	=	Reference value

Operators

$<\cdot>$	=	Time average
$\sigma_{\cdot}$	=	Standard Deviation
$\bar{\cdot}$	=	Area average
$\mathrm{Var}(\cdot)$	=	Variance

Greek symbols

α	=	Swirl angle, deg.
$\alpha_i(t)$	=	POD temporal coefficient for mode *i*
$\theta_{i,k}^{+}$	=	Positive circumferential extent in the *k*-th swirling region of the *i*-th ring
$\theta_{i,k}^{-}$	=	Negative circumferential extent in the *k*-th swirling region of the *i*-th ring
ρ	=	Fluid density
$\mu_{(X\wedge k,\ Y\wedge l,\ Z\wedge m)}$	=	Statistical moments of order *k*l*m*
Φ_i	=	Flow mode *i*
Ω_i	=	Collision operator

I. Introduction

Future aircraft engine configurations are expected to require a closer coupling between the propulsion system and the airframe, with potential benefits in terms of drag, noise and overall performance [1]. For many embedded and partially-embedded engine systems, the complexity of the flow field associated with convoluted intakes presents an area of notable research challenges. As the duct aerodynamics have greater importance for engine operability and performance [1] [2]. The convolution of the intake duct introduces flow distortion and unsteadiness which must be understood and quantified when designing the propulsion systems. Current industry practice for characterising distorted flow fields into compressor or fan systems specifies a number of intrusive pressure rakes to measure the time average distortions of the flow field introduced to them. This is known to have limitations for predicting instability onset [1]. Consequently, the risk may be carried forward into full scale testing which has been documented to demonstrate the impact that unknown distortion characteristics of an intake's design can cause major penalties on a development programme [1]. Although inlet distortion is typically quantified from the time-averaged distribution of total pressure and velocity at a given axial position upstream the engine face, previous studies noted that engine stall can be generated from distortion fluctuations [2] and highlighted the importance of the unsteadiness levels. Further studies of dynamic distortion emphasized the importance of instantaneous distortion and in particular the local peak values. For example, for an engine operating under steady operating conditions a stall was observed after several minutes, which indicates an association with an unsteady distortion characteristic [2].

The flow distortion associated with convoluted aero-engine intakes was assessed in numerous previous studies. Wellborn et al. [3] undertook an experimental characterisation of the flow through a diffusing S-duct configuration. The total pressure distribution at the Aerodynamic Interface Plane (AIP) showed a low-pressure zone on the lower part. Wall static pressure measurements and flow visualization demonstrated that this effect is associated with a large separation generated within the first part of the duct. The flow field also featured strong secondary flows which led to the generation of a pair of counter-rotating vortices located at the lower part of the AIP. High bandwidth pressure measurements in two S-duct configurations with different centreline offset were presented by Delot et al. [4] and Garnier et al. [5]. These measurements demonstrated notable unsteadiness generated by the separation region, which produced oscillations of the flow distortions at the exit plane. However, limited research has been done on the experimental characterisation of dynamic nature of flow distortion in such intakes with regards to the behaviour of key distortion descriptors. Delot et al. [6] first attempted the analysis of the instantaneous evolution of total-pressure distortion descriptors such as CDI, RDI and DC(60) using high temporal resolution measurement data. Zachos et al. [7] and Gil-Prieto et al. [8] [9] went further with the experimental investigation of the instantaneous relation between distortion descriptors using Stereoscopic Particle Image Velocimetry methods. These methods enabled for the first time a high resolution mapping of the velocity field at a cross flow plane at the exit plane of the S-duct. In the case of Gil-Prieto et al. [9], the PIV measurements were also resolved in time which enabled the spectral analysis of various flow features and their associated critical frequencies. These studies demonstrate that non-intrusive, optical methods for flow diagnostics are potentially a promising way forward in characterising complex flow fields in internal systems.

In terms of numerical predictive capability, a number of previous studies reported CFD results on various S-duct configurations. For example, Delot and Scharnhorst [10] and Fiola and Agarwal [11] showed that well established turbulence models like the Spalart-Allmaras and the k-ω Shear Stress Transport (SST) can reasonably capture the main flow physics of the highly separated flows within convoluted intakes. However, the same studies also noted that not all performance metrics such as total pressure recovery or swirl distortion could be accurately captured by these models. Higher fidelity studies were presented by Delot et al. [6] and Berens et al. [12] where the capability of Detached Eddy Simulations (DES) to capture the unsteady nature of flow separations that occur within the serpentine ducts was demonstrated.

An alternative, less computationally expensive than Delot's method was presented by Watson at al. [13]. In this study a zonal RANS/LES approach was developed to predict the unsteady flow within the S-duct intakes previously studied by Wellborn et al. [2] and Garnier et al. [5]. In this work, Reynolds Averaged Navier Stokes equations were applied close to the walls of the computational domain whereas Large Eddy Simulation (LES) is used for the inner flow zones. This approach enabled the relatively accurate representation of the flow unsteadiness produced by the separation region along with an accurate prediction of the separation point. As a result the associated resulting shear layers which affect the dynamic nature of the distortions presented further downstream at the AIP were also accurately captured. A study more focused on the unsteady total pressure and swirl distortion prediction was presented by MacManus et al. [14]. This work reported flow field predictions across a range of different S-duct configurations using a Delayed Detached Eddy Simulation (DDES) approach which was also compared to reference RANS simulations. The study examined the effects of inlet Mach and Reynolds numbers on the unsteady total pressure and swirl distortion characteristics at the S-duct exit to conclude that none of the above caused notable variations in the peak swirl

distortion metrics at the AIP. However, the same study established that an increase in the inlet Mach number reduces the duct pressure recovery with a modest increase in the average DC(60) total pressure distortion descriptor. Proper Orthogonal Decomposition (POD) was applied to identify the underpinning flow modes associated with the overall distribution of unsteadiness. Spectral analysis of the POD temporal coefficients was also performed as part of the work which identified the key modes that shared common characteristics with the unsteady signatures of the total pressure spectral signatures. Further DDES work was presented by Gil-Prieto et al. [15] where POD was applied to identify the main coherent structures within the unsteady flow field of an S-duct intake. The numerical computations were initially validated against PIV measurements that were available at the exit plane of the S-duct (AIP). The DDES data, decomposed by means of a POD method, was then used to identify the two main unsteady flow mechanisms that dominate the flow field, a lateral swirl switching mode and vertical switching mode both of which shed from the flow separation region within the duct. These structures were ultimately linked to the modulation of the main loss region and the unsteady velocity gradient variations at the AIP.

The unsteady flow prediction within S-duct intakes has also become a focal point of a number of AIAA's Propulsion Aerodynamics Workshops (PAW). As part of the 3rd AIAA PAW, the predictive capability of a large number of solvers for an S-duct case was presented. A summary of these results was reported by Winkler and Davis in [16]. The portfolio of cases included a baseline S-duct configuration previously studied by McMillan et al. [17] and a number of variations of it that included the presence of an AIP pressure probe rake or flow control vortex generators as part of the computational domain aiming to assess their impact on the flow field. A number of flow solvers was tested on common grids and flow conditions that were provided to the participants. The results were primarily focused on the flow characteristics and total pressure distortion at the AIP for the various S-duct configurations and indicated that the DDES approach yields more representative results in terms of overall loss prediction. This enables a more accurate calculation of main flow distortion parameters such as the overall pressure recovery coefficient. However, no further assessment of additional distortion descriptors was included in these evaluations and as such the predictive capabilities of these computational tools with regards to the full portfolio of unsteady swirl and total pressure distortion descriptors remains unclear despite the fact that this was highlighted as a key requirement.

Finally, a lattice Boltzmann simulation approach to predict the unsteady characteristics of the flow within an S-duct intake was presented by Noetling et al. [18]. In this study the S-duct configuration previously studied by Harloff et al. [19] was used. This was effectively the Wellborn original design [3] coupled with a nose cone. An unsteady simulation approach was applied, analogous to a hybrid URANS-LES formulation. As part of the study, a baseline configuration as well as a configuration that included vortex generation for passive flow control were looked at and the numerical results were compared against experimental data by Delot et al. [4]. The analysis of the numerical results was focused on the capability of the lattice Boltzmann method (LBM) to accurately predict the onset and the size of the separation region within the intake. The total pressure recovery mean and unsteady profiles at the AIP were also reported in comparison to the test data. The study concluded that LBM was a fairly accurate tool for the unsteady simulations in S-duct type diffusers as the LBM predictions showed a maximum discrepancy of 0.3% from experimental total pressure recovery coefficients for the configurations tested. However, no evidence was provided with regards to its capability to capture the unsteady total pressure and swirl distortion characteristics at the AIP. These are of critical importance to determine whether such an approach can be viable for further industrial use in particular for flow predictions in coupled intake – fan systems. Current state of the art lattice Boltzmann solvers are arguable able to predict flow topologies in the highly compressible regime which was a short coming of previous LBM implementations. This could offer significant benefits to the modelling of various propulsion sub-systems which traditionally operate at high subsonic speeds including S-shaped intakes where the inlet Mach number is typically in the range between 0.6 – 0.85. However, solver validation remains a key requirement especially when the examined flow system is by nature highly unsteady as in the example of S-duct intakes.

Within this context, the aim of the current work is to investigate the capabilities of a modern LBM implementation to characterise the unsteady features of the distorted flow field within S-duct aero engine intakes. This paper presents the application of a lattice Boltzmann method for unsteady flow distortion predictions at the exit plane of a previously studied S-duct configuration. The main features that potentially make such an approach attractive for unsteady flow predictions are the low computational cost and the minimum meshing requirements compared to conventional LES or DES approaches. The numerical results are validated against time-resolved stereoscopic PIV (TR-PIV) data for the same S-duct configuration. The analysis is focused on the dynamic swirl distortion predictions and the characteristics of the unsteady signals of key swirl distortion descriptors at the AIP. The dynamic behaviour of the swirl distortion metrics is finally linked to the main flow mechanisms via the application of a Proper Orthogonal Decomposition of the flow. Ultimately, the capability of the LBM solver to capture the flow physics of highly distorted flows is evaluated, aiming to determine the applicability of such methods to the simulation of coupled fan-intake configurations whose current high computational cost prohibits wider use.

II. Methodology

A. S-duct configurations

In this research the high offset S-shaped intake previously studied by Garnier [5], Zachos et al. [7] and Gil-Prieto et al. [8] was used for the LBM simulations and the experimental campaigns (Figure 1). The intake has a centreline vertical offset of h/L=0.49, an area ratio of A_{out}/A_{in}=1.52 and an AIP dimeter of D_{AIP}=150 mm. (see Figure 1). The tests and simulations were performed at an inlet centreline Mach number of M_{ref}=0.27 which corresponds to an inlet Reynolds number of Re_{Din}=7.1 x 10^5. The inlet Mach number during the test campaigns was measured at a reference plane located $1.45D_{in}$ upstream of the inlet plane of the S-duct. The AIP was located $0.24D_{out}$ downstream of the exit plane of the S-duct.

B. Lattice-Boltzmann CFD modelling

For the CFD simulations the commercial software SIMULIA XFlow was employed. The implementation is based on a Lattice Boltzmann method (LBM) and uses a multiple-relaxation-time scheme with a scattering operator implemented in central moment space [20] [21]. The time-stepping model is based on a propagate-collide scheme, on top of a lattice discretization. The propagation step performed on a lattice enforces a constant time step *dt* and a discrete set of velocities ($e_i \; i = 1, \dots, b$) that ensure that the positions of the simulated particles motion is restricted to lattice sites. The set of velocities thus generates the lattice, and for each lattice site, *b* probability distribution functions (PDFs) $f_i(\boldsymbol{r}, t)$ are stored. The three-dimensional lattice structure employed by XFlow includes 27 velocity directions, thus providing a higher-order spatial discretization scheme than the traditional LBM codes. In the continuum space (with discrete velocities), the Boltzmann transport equation can be written as follows:

$$\frac{\partial f_i}{\partial t} + \boldsymbol{e}_i \cdot \nabla f_i = \Omega_i, \qquad i = 1, \dots, b \tag{1}$$

Where Ω_i is the collision operator that computes a post-collision state conserving mass and linear momentum. The stream-and-collide scheme of the LBM can be interpreted as a discrete approximation of the continuous Boltzmann equation. The streaming or propagation step models the advection of the particle distribution functions along discrete directions, whereas most of the physical phenomena are modelled by the collision operator, which also has a strong impact on the numerical stability of the scheme.

The collision operator is generally modelled as a relaxation of the PDFs toward an equilibrium state. A single-relaxation time (SRT) based on the Bhatnagar–Gross–Krook approximation is used in the most common approach. However, the SRT collision operator, although still commonly used for many applications, has several shortcomings that preclude its use for high Mach number studies or make it unstable if low viscosities are employed. To address some of the BGK limitations multiple-relaxation-time (MRT) collision operators have been introduced [22], where the collision process is carried out in momentum space instead of the usual velocity space. As in the continuum Boltzmann equation, the statistical moments of the Probability Density Functions (PDFs) are used to recover the macroscopic flow properties. For example, the fluid density is obtained from the zero order moment, i.e. the sum of the PDFs over the discrete velocity directions. Similarly, the linear momentum is obtained from the sum of the PDFs times the velocity vector as follows:

$$\rho = \sum_{i=1}^{b} f_i \qquad ; \qquad \rho \boldsymbol{v} = \sum_{\boldsymbol{i=1}}^{\boldsymbol{b}} f_i \boldsymbol{e}_i \tag{2}$$

The relation between the PDFs f_i and the raw moments $\mu_{X^k Y^l Z^m}$, a set of which will be denoted by μ_i, can be expressed in matrix form:

$$\mu_i = M_{ij} f_j \tag{3}$$

where the raw moments are defined as:

$$\mu_{X^k Y^l Z^m} = \sum_i^N f_i \, e_{ix}^k e_{iy}^l e_{iz}^m \tag{4}$$

The MRT collision operators can then be expressed as a relaxation in momentum space followed by the inverse transformation to the density function space:

$$\Omega_i^{MRT} = M_{ij}^{-1} \hat{S}_{ij} \left(\mu_i^{eq} - \mu_i \right) \tag{5}$$

The collision matrix $\hat{S}_{ij}$(equivalent to $1/\tau$ in the SRT collision operator) is diagonal, $\mu_i^{eq}$is the equilibrium value (generally derived from a Maxwell–Boltzmann distribution with the same macroscopic variables of the pre-collision state) of the momentum, μ_i, and M_{ij} is the transformation matrix [23].

For the LBM approach used in this work, the collision operator is based on a multiple-relaxation time scheme. A modification on the standard implementation is introduced by computing the scattering operator in central momentum space rather than in the raw moment one. By shifting the discrete particle velocities with the local macroscopic velocity, the Galilean invariance and the numerical stability for a given velocity set are greatly improved [24] [25]. The Mach number limitation is also enhanced, and global Mach number up to 0.6 can be handled, whereas the local Mach number is limited to 1.0. A large-eddy simulation (LES) scheme is used to model sub-grid turbulence, introducing an additional turbulent eddy viscosity, ν_t. Specifically, the wall-adapting local eddy (WALE) viscosity model is used, which provides a consistent local eddy viscosity and near-wall behaviour [26]. The boundary layer region is modelled by a generalized law of wall given by Shih et al. [27] based on a previous work of Tennekes and Lumley [28], approach that takes into account the effect of both adverse and favourable pressure gradients. The LBM formulation has already been successfully applied to the analysis of a variety of highly turbulent flows, such as high-lift wing configuration [29] [30], complex landing gear geometries (including noise prediction) [31] and dynamic manoeuvres [32].

For the LBM simulations the computational domain shown in Figure 1 was developed. A velocity inlet boundary condition was imposed $3D_{in}$ upstream the inlet plane of the S-duct to prescribe an inlet Mach number of M_{ref}=0.27. That was combined with a non-reflecting gauge pressure outlet with a relaxation parameter of 0.5 that was prescribed $5D_{out}$ downstream of the exit plane of the S-duct (Figure 1). The latter was required to damp out the unsteady pressure waves created in the fluid domain during the run time by the inlet velocity condition due to the mildly compressible nature of the LBM solver. A non-uniform lattice resolution was used with a local refinement near the walls that provides a maximum y+ value of 100 across the entire domain of interest (Figure 2). In order to achieve a fully established unsteady solution, a total simulation time of 0.657 s was set, which corresponds to approximately 100 through-flow (convective) times calculated based on the mean axial velocity at the reference plane and the length of the S-duct mean line. Only the last 40 convective times were considered for the post-processing in order to avoid the initial transient part of the simulation from the steady to the established unsteady solution. A time-step, *dt*, of 1.25e-06 s at the finest scale was used. A grid of 1,440 nodes across the Aerodynamic Interface Plane (AIP) were monitored during the simulation, which were arranged in 72 equi-spaced rakes and 20 equispaced circumferential rings. The three-component velocity vector, static pressure and static temperature were extracted from the AIP probes every one time-step which resulted in an output unsteady signal of these properties of approximately 130 kHz at each AIP probe. The flow data was further processed by a bespoke flow distortion processing platform (see Refs. [7], [8], [9]and [15]).

C. Experimental configuration and methods

The high offset S-duct configuration shown in Figure 1 was used for the measurements. The facility is described in detail by Zachos et al. [7]. Time-resolved, stereoscopic PIV (TR-PIV) was used to measure the AIP velocity fields across a range of reference Mach numbers at the inlet of the S-duct between M_{ref}=0.27-0.6 as shown by Gil-Prieto et al. [9]. A dual cavity pulsed Nd:YAG laser was used to illuminate the measurement plane at the AIP, located $0.24D_{out}$ downstream of the exit plane of the intake. Two high-speed CMOS cameras with a sensor resolution of 1280x800 px^2 were used for the flow imaging in stereo optical arrangement. The acquisition frequency was 4 kHz, and 20,000 snapshots per dataset were acquired as this was previously found sufficient to achieve statistically converged results [9]. A direct correlation method was used, with a search window of 32x32 px^2 and 50% overlap. That resulted in approximately 1,800 velocity vectors across the measurement plane and a spatial resolution of approximately 2.7 mm^2. The uncertainty of the 3 dimensional reconstructed velocity vector was 5% of the time-averaged and area-averaged out-of-plane velocity at the AIP [9].

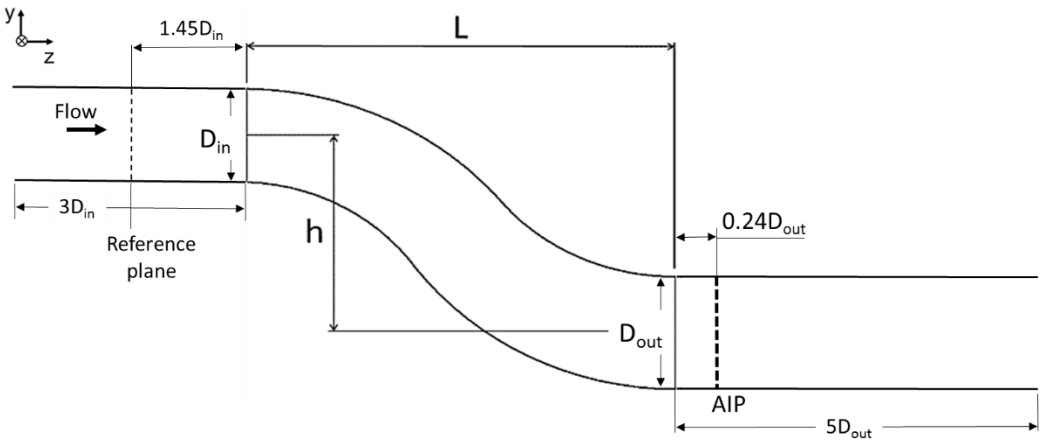

Parameter	High offset S-duct
A_{out}/A_{in}	1.52
L/D_{in}	4.95
h/L	0.49
D_{out} [mm]	150.0

Figure 1. Parametric definition of the S-shaped intake and key domain dimensions.

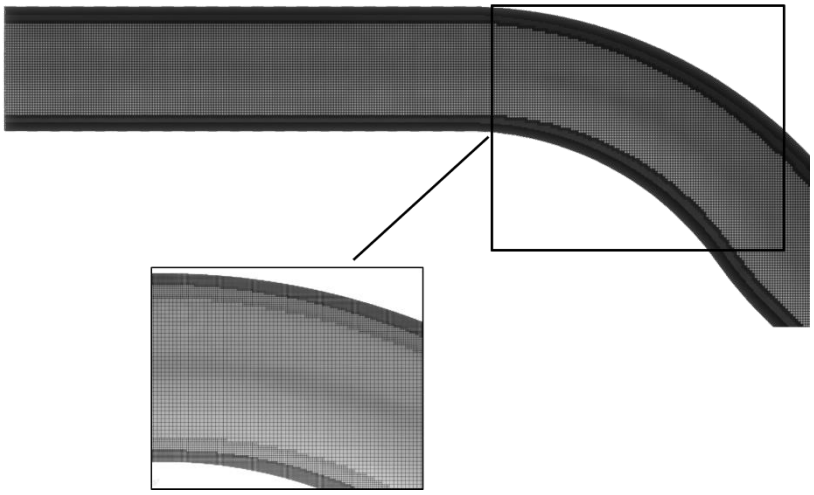

Figure 2. Lattice structure showing the refined near-wall regions.

III. Results and discussion

A. Time averaged and unsteady flow field analysis

Time-averaged velocity distributions at the AIP are shown in Figure 3 as predicted by the LBM and are compared to the TR-PIV data. In all figures hereafter, *u* is used to indicate the horizontal, in-plane velocity along the *x*-axis, *v* the vertical in-plane component along the *y*-axis and *w* the out-of-plane component along the axial direction (*z*-axis). These mean flow statistics have been discussed in detail previously by Zachos et al. [7] and Gil-Prieto et al. [9], and only the key aspects will be addressed herein. The high loss region arises at the lower part of the AIP and shown in the non-dimensional, mean out-of-plane velocity distributions of the LBM (Figure 3a) and TR-PIV datasets (Figure 3e). It is of note that the extent of the low out-of-plane velocity zone predicted by the LBM simulations is around 20% larger than the TR-PIV measurements. The LBM calculated axial velocity deficit ($\langle w \rangle / \langle \overline{w} \rangle_{AIP}$) reaches a value of 0.8 whereas the measured minimum was between 0.9-1.0. Better agreement between LBM and TR-PIV is shown in the horizontal velocity component (*u*-velocity, Figure 3b and f) where both datasets indicate similar u-velocity topologies across the plane. With regards to the vertical velocity component (v-velocity) a low velocity zone is shown in the experimental data at the top part of the AIP (Figure 3g) whereas no such flow regime is predicted by the LBM simulations (Figure 3c). Finally, the calculated and measured swirl angle distributions show the twin vortical structures located at the lower half of the plane (Figure 3d and h).

The unsteadiness of the various flow components was evaluated based on the instantaneous velocity snapshots from both approaches. In all cases, the LBM simulations indicated notably lower levels of unsteady flow across the AIP than the TR-PIV data (Figure 4). The discrepancy in the unsteady swirl angle distributions, σ_α, between the LBM method and the test data is of particular note. The LBM under-predicted the unsteady swirl angle fluctuations by approximately 30%-40% (Figure 4d and h) compared to the TR-PIV. This is of key importance to the prediction of the peak distortion events that will be further shown in section C. These extreme distortion events were previously known of causing instabilities in the operation of a fan system [9]. A possible cause of the LBM under predictions of the unsteady flow distributions is the non-reflecting boundary condition that was applied at the exit of the domain in order to ensure convergence of the numerical scheme and was also previously found to damp the unsteady flow fluctuations. Improvements on LBM's predictive capability for such flows is an aspect of ongoing work.

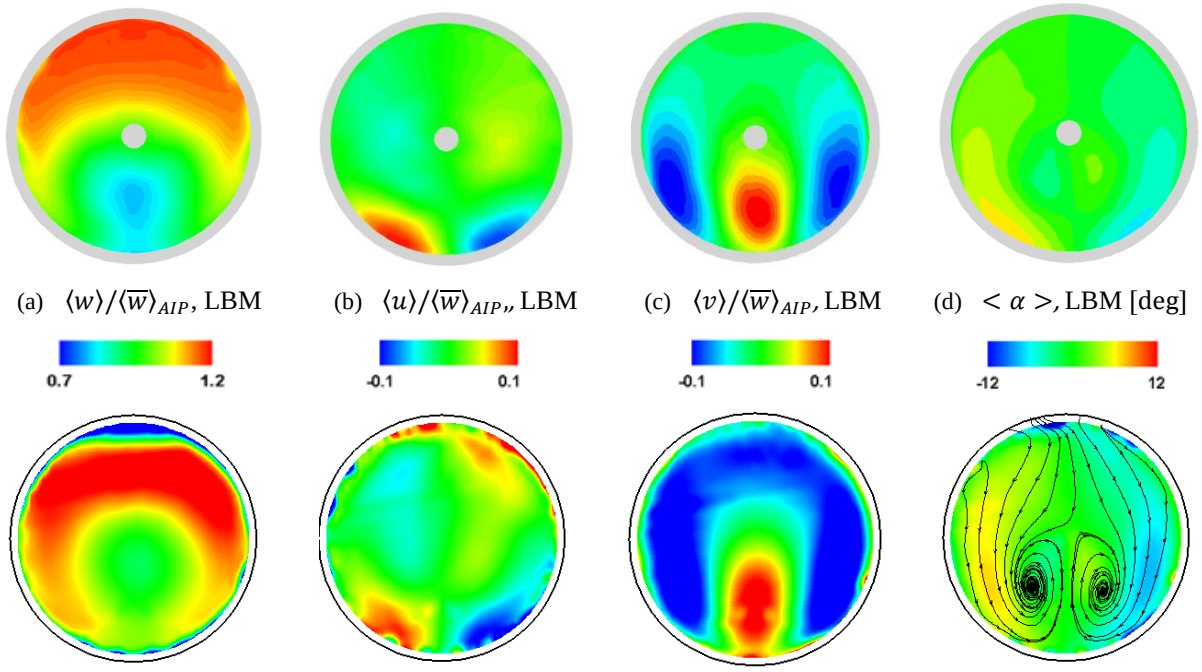

(a) $\langle w \rangle / \langle \overline{w} \rangle_{AIP}$, LBM (b) $\langle u \rangle / \langle \overline{w} \rangle_{AIP}$,, LBM (c) $\langle v \rangle / \langle \overline{w} \rangle_{AIP}$, LBM (d) $< \alpha >$, LBM [deg]

(e) $\langle w \rangle / \langle \overline{w} \rangle_{AIP}$, TR-PIV (f) $\langle u \rangle / \langle \overline{w} \rangle_{AIP}$, TR-PIV (g) $\langle v \rangle / \langle \overline{w} \rangle_{AIP}$, TR-PIV (h) $< \alpha >$, TR-PIV [deg]

Figure 3. LBM and TR-PIV AIP time-averaged flow field for the S-duct with h/L=0.49 at M_{ref}=0.27.

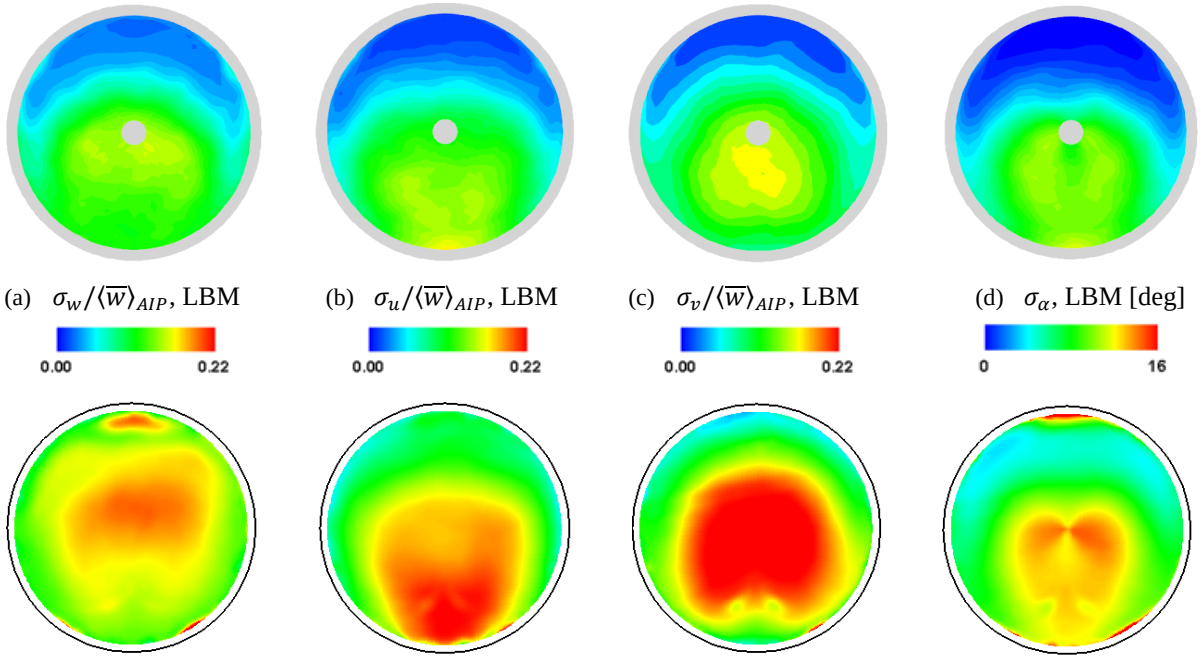

(a) $\sigma_w/\langle\overline{w}\rangle_{AIP}$, LBM (b) $\sigma_u/\langle\overline{w}\rangle_{AIP}$, LBM (c) $\sigma_v/\langle\overline{w}\rangle_{AIP}$, LBM (d) σ_α, LBM [deg]

(e) $\sigma_w/\langle\overline{w}\rangle_{AIP}$, TR-PIV (f) $\sigma_u/\langle\overline{w}\rangle_{AIP}$, TR-PIV (g) $\sigma_v/\langle\overline{w}\rangle_{AIP}$, TR-PIV (h) σ_α, TR-PIV [deg]

Figure 4. LBM and TR-PIV unsteady AIP flow field for the S-duct with h/L=0.49 at M_{ref}=0.27.

B. Unsteady Proper Orthogonal Decomposition

Coherent structure identification was conducted via a Proper Orthogonal Decomposition (POD) approach for both the numerical as well as the experimental data. POD enables the identification of underpinning, unsteady flow topologies that may exist within a flow field. This analysis method was previously demonstrated on S-duct data [8] [9] [15] but is a widely applied method also shown in other types of flows [33]. The methodology decomposes the flow field of interest into a set of orthogonal bases, constant over time, called modes (Φ_i). With each mode, a temporal coefficient is also identified $a_i(t)$, and the energy contribution associated with that mode ($a_i(t)\Phi_i$). The method then allows representing the flow field with a number $\boldsymbol{k}$ of modal contributions V_{1-k} (Eq. 6). The contribution of each mode to the area and time-averaged TKE (Eq. 7) is obtained by means of the variance of the temporal coefficient $Var(\alpha_i)$ (Eq. 7). The results then are ordered based on their TKE contribution to the overall energy levels.

$$\boldsymbol{V}_{1-k} = \langle \boldsymbol{V} \rangle + \sum_{i=1}^{k} a_i(t)\, \boldsymbol{\Phi_i}(x,y) \tag{6}$$

$$\langle \overline{TKE} \rangle_{1-k} = \sum_{i=1}^{k} Var(\alpha_i) \tag{7}$$

Gil-Prieto et al. previously showed a POD based analysis using experimental data acquired at the AIP of an S-duct intake configuration at M_{ref}=0.6 [9]. In this analysis the first four POD modes of the flow field were identified as the most energetic ones containing around 30% of the overall Turbulent Kinetic Energy of the original flow field. The identified modes were classified into two lateral and two vertical oscillatory modes whose frequency spectra were correlated with the temporal characteristics of the velocity components. This enabled the quantification of the relative contribution of each POD mode into the overall unsteady content of the flow. For example, the maximum unsteady contributions of the switching modes' temporal coefficients were found at a Strouhal number of around St=0.42. This frequency was also associated with an out-of-phase lateral oscillation of the w-velocity component at each side of the vertical symmetry axis of the AIP.

The first four POD modes extracted from the LBM numerical data are shown in Figure 5 for the high offset S-duct configuration with h/L=0.49 at M_{ref}=0.27. These show similar characteristics as the TR-PIV data as well as with the POD modes for the same S-duct at M_{ref}=0.6 previously presented by Gil-Prieto et al. [9]. The FVM, whose contribution to the total TKE is 14.0% and 12.6% for the LBM and TR-PIV results respectively, was found to be the most energetic mode in both cases. The SVM's contribution to the TKE was found around 4.5% for the LBM and 5.8% for the experimental case. The First and Second Vertical Modes (FVM and SVM, Figure 5a to d and Figure 5i to l respectively) represent a vertical out-of-plane velocity fluctuation located centrally at the AIP with significant frequency contributions between St=0.5-1.0 (see Figure 6a and c). These are shown in both the LBM and TR-PIV datasets. Significant contributions across the same frequency range were previously detected in the spectral analysis of the velocity components by Gil-Prieto et al. [9]. More distinctive features are shown by the First and Second Switching Modes (FSM and SSM, see Figure 5e to h and Figure 5m to o respectively). The switching modes together represent perturbations at the AIP shown as vortical patterns alternating between co- and counter-rotating bulk swirls at a specific frequency. This feature is attributed to the instabilities of the secondary flows developing within the duct which result in the formation of a pair of Dean vortices at the AIP. The dominant frequency of the switching modes was identified at St=0.51 (Figure 6b and d) with a more distinct peak than the vertical modes. This seems to be in partial agreement with previous TR-PIV results presented by Gil-Prieto et al. [9] for the same S-duct configuration at M_{ref}=0.6 where the peak switching mode frequency was detected at St=0.42 based on TR-PIV measurements. In terms of the switching mode contribution to the overall TKE, the FSM was found at 11.2% for the LBM and 10.5% for the TR-PIV results whereas the SSM contributions were 6.0% for the LBM and 4.0% for the experimental dataset respectively.

Overall, there is a useful level of agreement between the LBM and the TR-PIV results in terms of the POD mode characteristics (Figure 5). The LBM PSD agreed with the TR-PIV results within 3% in terms of the FSM peak St number (Figure 6). Partial agreement was shown in the FVM St number range which is, however, more broadband with less distinct frequency peaks (see also Ref. [9]). LBM predicted a slightly wider range of high St numbers between 0.2-1.25 (Figure 6a) whereas the TR-PIV PSD indicates this band across a range between St=0.5-1.0 (Figure 6c).

High-offset S-duct (h/L=0.49) – M_{ref}=0.27

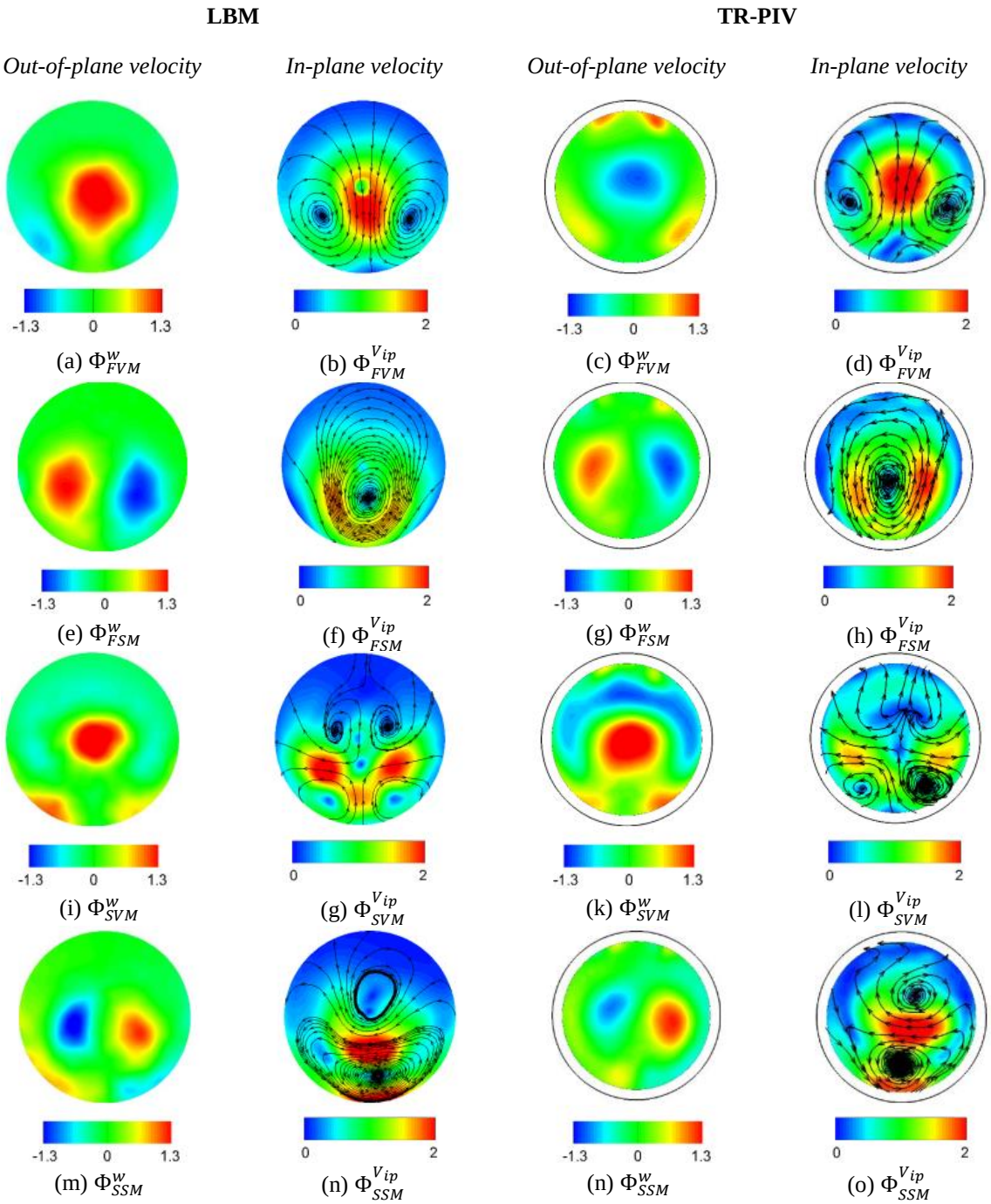

Figure 5. POD models of the AIP velocity field for the S-duct with h/L=0.49 at M_{ref}=0.27.

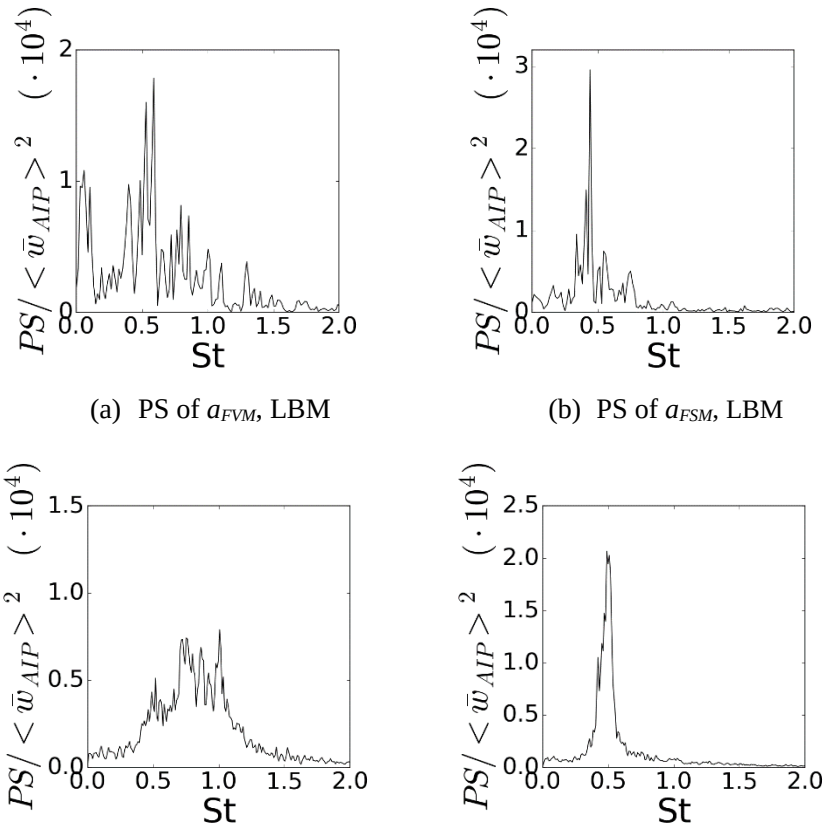

(a) PS of a_{FVM}, LBM

(b) PS of a_{FSM}, LBM

(c) PS of a_{FVM}, TR-PIV

(d) PS of a_{FSM}, TR-PIV

Figure 6. Spectral content of the POD temporal coefficients obtained by LBM and TR-PIV data for the S-duct at M_{ref}=0.27.

C. Unsteady distortion characteristics

For the analysis of the unsteady distortion characteristics a number of established swirl distortion descriptors was used [34]. In these definitions the AIP is divided into a number of radial rings where the distortion descriptors are evaluated. The distortion descriptors are evaluated on the basis of a twice-per-revolution swirl pattern which is shown in Figure 7. Swirl angle is positive in the counter-clockwise direction when the AIP is viewed from downstream. Positive and negative circumferential extents, $\theta_{i,k}^{+}$and $\theta_{i,k}^{-}$ define the size of the *k*-th swirling region in the *i*-th ring. Positive and negative sector swirls $SS_{i,k}^{+}$ and $SS_{i,k}^{-}$ are defined as the mean swirl-angle value in each of the m swirling regions. Sector swirl and extents are used as the foundation for the development of a range of swirl descriptors used to quantify the nature and strength of the swirl distortion [34]. Swirl intensity (SI) reflects the averaged absolute swirl angle in each radial ring (Eq. 8). Swirl directivity (SD) shows the overall sense of rotation of the swirling flow (Eq. 9 and Figure 8) and Swirl Pairs (SP) indicates the number of swirl pairs relative to the swirl region in the ring which encloses the highest absolute swirl angle content, $max\left(SS_{i,k}^{+}\theta_{i,k}^{+}, \left|SS_{i,k}^{-}\theta_{i,k}^{-}\right|\right)$ (Eq. 10 and Figure 9). The swirl descriptors were evaluated at five equal area rings that makes it consistent with common industrial practice based on conventional pressure probes that are used to measure the distortion patterns [34]. At each ring, 72 equi-spaced circumferential points are considered, which results in an azimuthal resolution of 5 deg.

An additional parameter that is introduced in these two dimensional distortion maps is the relative frequency of occurrence of these instantaneous distortion events. This frequency enables the generation of Joint Probability Density Function (j-PDF) distortion maps. For the calculation of the j-PDF, the range for each distortion descriptor was discretised in 60 equal partitions which resulted in a resolution of approximately 0.03 for SP and SD. The probability to identify the distorted pattern within a given region of this SP-SD map is obtained by integration of the PDF over the desired area (Eq. 11). The j-PDF distortion map representation offers an alternative assessment of the unsteady distortion topologies that develop across the AIP which are known to present notable variations from the time-averaged representation that is typically reported.

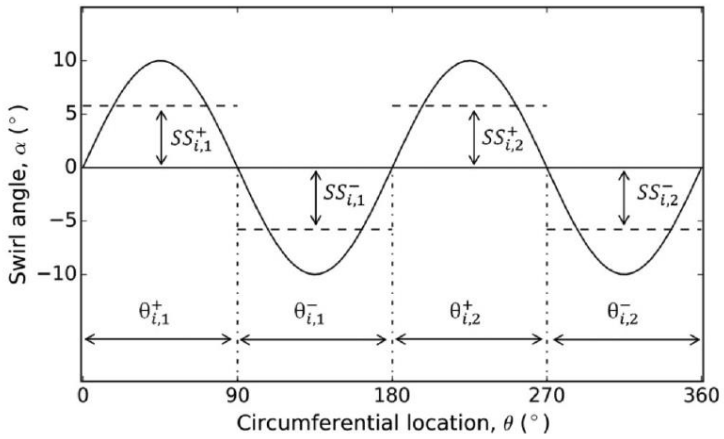

Figure 7. Twice-per-revolution swirl distortion pattern based on Ref. [34].

$$SI(i) = \frac{\sum_{k=1}^{m} SS_{i,k}^{+} \cdot \theta_{i,k}^{+} + \sum_{k=1}^{m} \left|SS_{i,k}^{-}\right| \cdot \theta_{i,k}^{-}}{360} \tag{8}$$

$$SD(i) = \frac{\sum_{k=1}^{m} SS_{i,k}^{+} \cdot \theta_{i,k}^{+} + \sum_{k=1}^{m} SS_{i,k}^{-} \cdot \theta_{i,k}^{-}}{\sum_{k=1}^{m} SS_{i,k}^{+} \cdot \theta_{i,k}^{+} + \sum_{k=1}^{m} \left|SS_{i,k}^{-}\right| \cdot \theta_{i,k}^{-}} \tag{9}$$

$$SP(i) = \frac{\sum_{k=1}^{m} SS_{i,k}^{+} \cdot \theta_{i,k}^{+} + \sum_{k=1}^{m} \left|SS_{i,k}^{-}\right| \cdot \theta_{i,k}^{-}}{2 \cdot Max\left\{ SS_{i,k}^{+} \cdot \theta_{i,k}^{+},\ \left|SS_{i,k}^{-} \cdot \theta_{i,k}^{-}\right| \right\}_{k=1,\ldots,m}} \tag{10}$$

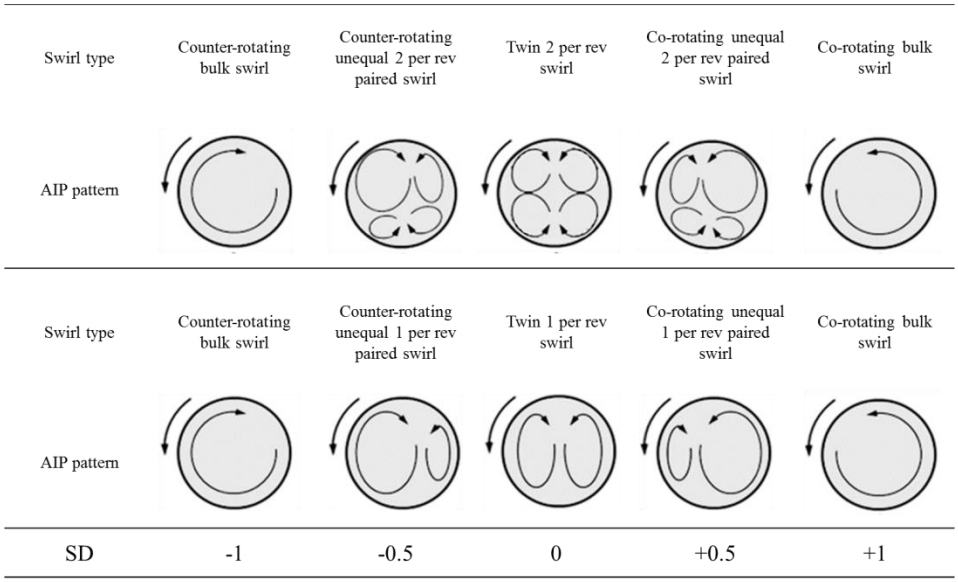

Figure 8. Swirl directivity (SD) spectrum for multiple per-revolution swirl distortion compared to a one-per-revolution pattern based on Ref. [34].

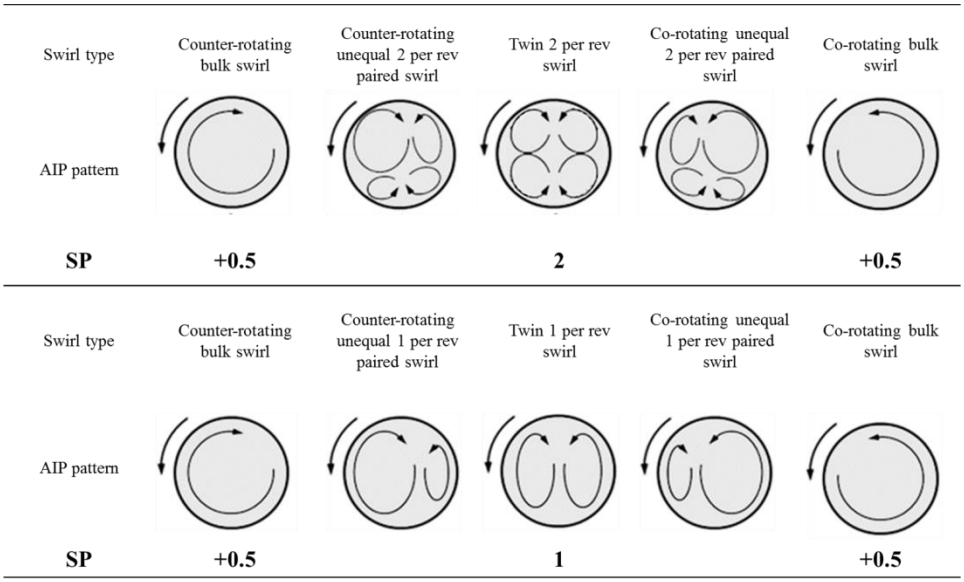

Figure 9. Swirl pairs (SP) spectrum for multiple per-revolution swirl distortion compared to a one-per-revolution pattern based on Ref. [34].

The distortion maps were generated at two representative radial positions at the exit plane of the intake; near the hub with r/R=0.316 and near the tip region (r/R=0.837). In this way any discrete distortion feature between these two span wise positions would be quantified. At the hub region with r/R=0.316 high relative frequency distortion events are detected at the two extremes of the domain where positive (SP=0.5 – SD=+1) or negative bulk swirl events (SP=0.5 – SD= -1) dominate the AIP flow topology (Figure 10). A symmetrical mode in between the two extreme ones showing the typical twin vortex topology symmetrically positioned with regards to the vertical AIP axis is also indicated with SP=1 – SD=0. This observation is in agreement with past results presented by Gil-Prieto et al. in Ref. [9] for this S-duct at a higher inlet Mach number of M_{ref}=0.6. The hub j-PDF maps suggest that the distorted flow oscillates predominantly between two extreme bulk conditions through a symmetric swirl pattern with SP=1 and SD=0. This behaviour is evident in both the LBM as well as the TR-PIV datasets (Figure 10a and c, respectively). Similar

observations can be made for the near tip position with r/R=0.837 where the j-PDF maps suggest a strong preference of the flow to remain along the same path with two extreme bulk swirl events and a symmetric twin vortex pattern in between. The extreme bulk swirl events are slightly less pronounced in the LBM dataset which indicate a longer residence of the flow around the vicinity of the twin symmetrical pattern. Nevertheless, both LBM and TR-PIV datasets are aligned with regards to the representation of the highest probability flow patterns at both radial positions.

$$P(SD_A \leq SD < SD_B, SP_A \leq SP < SP_B) = \int_{SP_A}^{SP_B} \int_{SD_A}^{SD_B} PDF \; dSD \; dSP \tag{11}$$

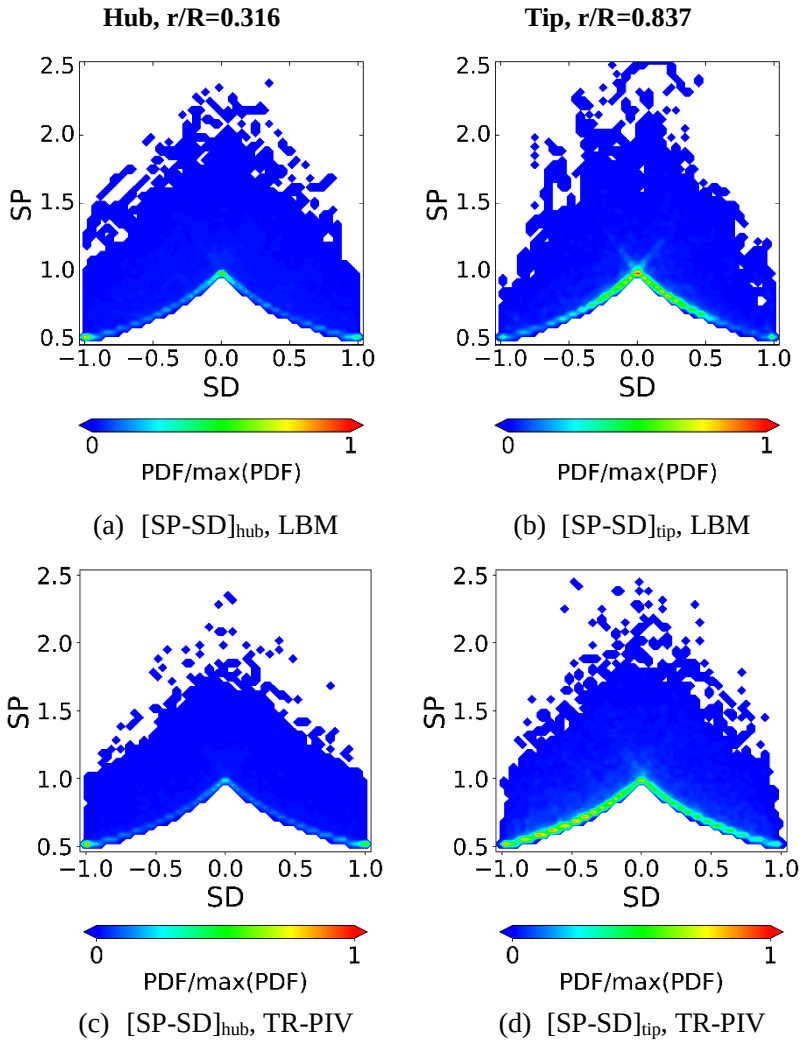

(a) $[SP\text{-}SD]_{hub}$, LBM (b) $[SP\text{-}SD]_{tip}$, LBM

(c) $[SP\text{-}SD]_{hub}$, TR-PIV (d) $[SP\text{-}SD]_{tip}$, TR-PIV

Figure 10. LBM and TR-PIV SP-SD j-PDF distortion maps at r/R=0.316 (hub) and r/R=0.837 (tip) for the S-duct at M_{ref}=0.27.

The distortion characteristics as illustrated by an SI-SP j-PDF map are also of note (Figure 11). Near the hub position (r/R=0.316) the SP range shown by the two datasets ranges between SP=0.5 (single bulk swirl) and SP= 2.0 (two vortex pairs). However, the LBM does not agree with the measurements in terms of the indicated range of SI. In the case of the TR-PIV dataset (Figure 11c) this was found as high as 27° whereas LBM (Figure 11a) suggests a narrower SI range with peak values not beyond the 20° threshold. The two datasets show better agreement in terms of the high probability regions of the SI-SP where bulk or twin vortex distortion events are indicated in both cases. Similar observations can be made about the tip region with r/R=0.837. In this region both approaches are in good agreement with regards to the SP range and also the high probability locus of distortion events which shows a high frequency swirl intensity of around SI=5-7°. However, LBM (Figure 11b) underestimates the peak SI events with a maximum of 10° whereas the TR-PIV measured maximum was around 15° at the tip (Figure 11d). This is a consequence of the LBM's under prediction on the swirl unsteadiness (see Figure 4). As previously described by Gil-Prieto et al. [35] and Tanguy et al. [36], these peak events may exceed the tolerance level of a propulsion system causing operability issues. As such, their characterisation for a coupled engine-intake system is of key importance to the specification of the system's operability range during operation, even if their probability of appearance is relatively low and stochastic. This remains the focal point of future work.

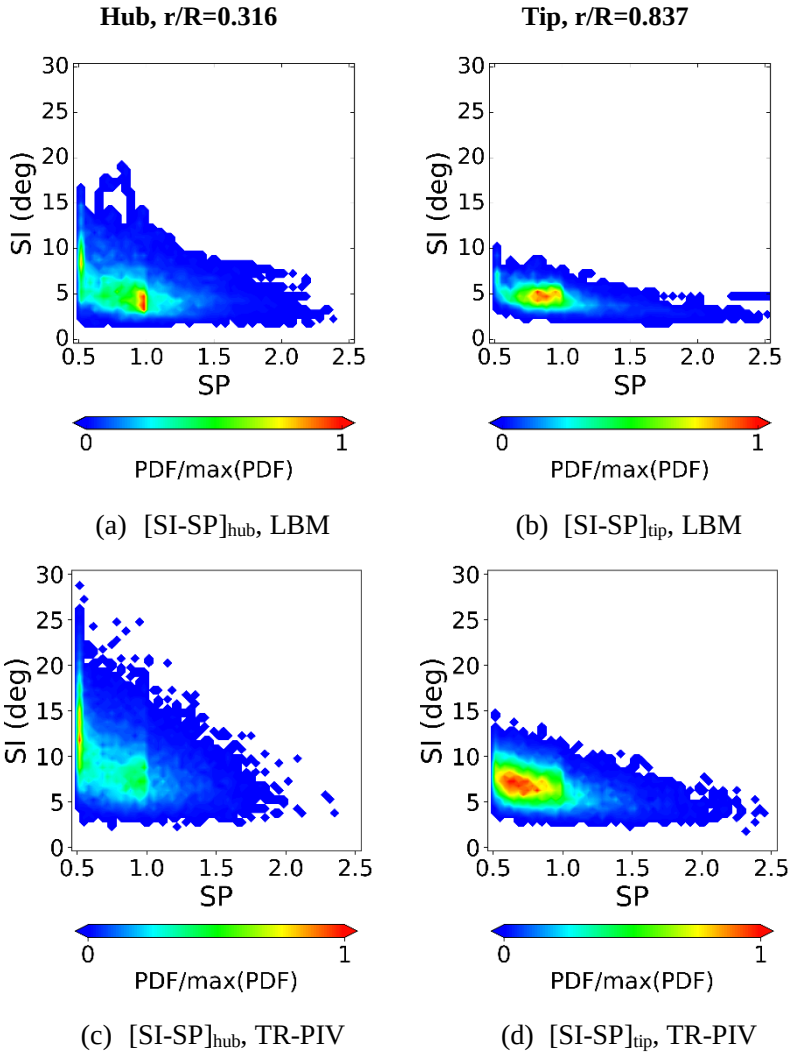

Figure 11. LBM and TR-PIV SI-SP j-PDF distortion maps at r/R=0.316 (hub) and r/R=0.837 (tip) for the S-duct at M_{ref}=0.27.

Finally, the temporal characteristics of the distortion descriptor signals from the LBM and TR-PIV datasets were analysed using spectral analysis. At both radial positions (r/R=0.316 and r/R=0.837), the LBM predicted SD signals showed notable contributions at around St=0.5 (Figure 12a and b). This is consistent with the dominant frequency related to the lateral switching modes FSM and SSM identified previously via the spectral analysis of the POD temporal coefficients (Figure 6). This observation correlates the unsteady behaviour of the SD descriptor with the underpinning lateral oscillations of the flow between two counter rotating bulk swirl events as shown in Figure 5. The LBM predicted temporal characteristics of the SD descriptor were also aligned with the TR-PIV data which indicated peak contributions at around St=0.5 at both hub and tip radial positions (Figure 12c and d).

The outcomes of the current analysis agree with Gil-Prieto's observations for the same S-duct at a higher inlet Mach number of M_{ref}=0.6 [9] which also suggested the weak dependency of the swirl distortion characteristics on the inlet Mach number. Overall, the LBM numerical approach successfully predicted the broad unsteady characteristics of the swirl distortion descriptors.

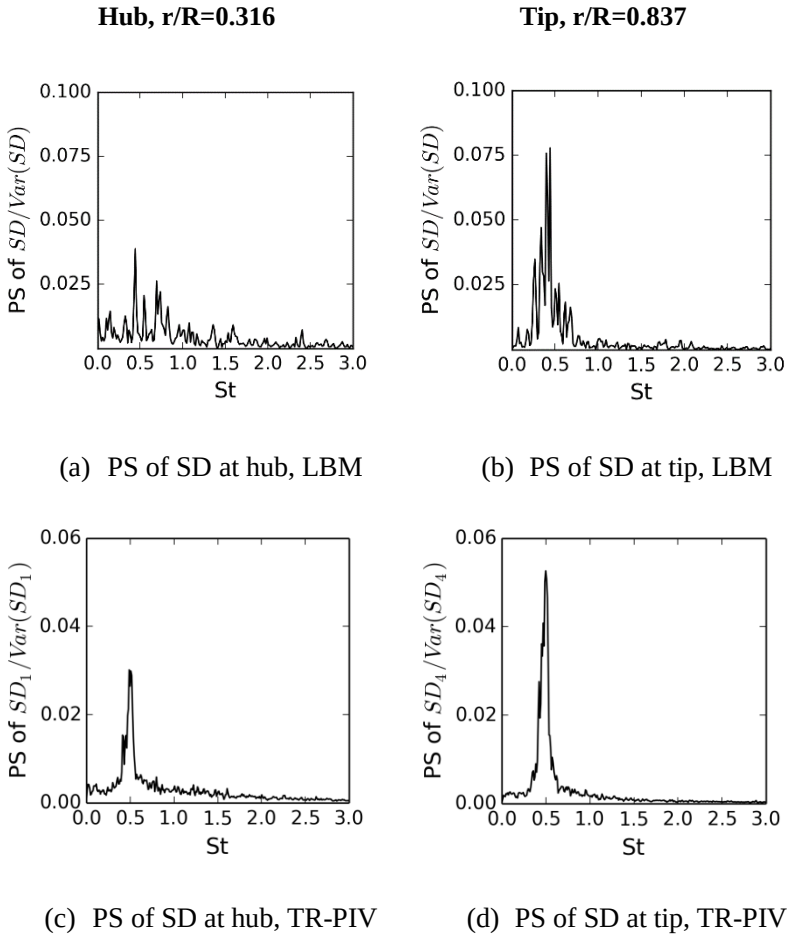

(a) PS of SD at hub, LBM (b) PS of SD at tip, LBM

(c) PS of SD at hub, TR-PIV (d) PS of SD at tip, TR-PIV

Figure 12. LBM and TR-PIV power spectrum content at r/R=0.316 (hub) and r/R=0.837 (tip) for the S-duct at M_{ref}=0.27.

IV. Conclusions

The unsteady swirl distortion characteristics of a complex aero-engine intake were investigated using TR-PIV and Lattice Boltzmann CFD methods. The flow was characterised at the exit plane (AIP) of a complex intake with a vertical offset to length ratio of h/L=0.49 and exit to inlet area ratio A_{out}/A_{in}=1.52 at an inlet reference Mach number of M_{ref}=0.27. The TR-PIV experimental approach enabled a spatial resolution of around 50 times higher than the conventional intrusive approaches that are historically used to quantify cross flow inlet distortion. The temporal resolution of 4 kHz that was used for the current work enabled the spectral analysis of the flow and distortion characteristics against which the Lattice-Boltzmann CFD solver was evaluated.

The current work shows the potential of Lattice-Boltzmann CFD methods to predict the unsteady flow and swirl distortion characteristics of flows within complex aero-engine intakes. More work is required to understand the disagreements between the magnitude of the predicted and measured unsteadiness. This is an area of ongoing research. Application of POD to the LBM unsteady data reveals the same underpinning flow modes that were found in the TR-PIV data, which suggests that the computational method predicts well the physics associated with the origins of the AIP unsteady characteristics namely the development of the separation and the propagation of shear layers within the S-duct. Finally, the j-PDF swirl distortion maps generated using the LBM unsteady data, show good agreement with the TR-PIV results indicating the applicability of Lattice-Boltzmann based methods to produce unsteady swirl distortion histories for S-duct intakes. Overall, the known weak dependency of the unsteadiness upon the inlet reference Mach number, the minimum mesh requirement and the fast convergence of the solver suggest the lattice Boltzmann methods are potentially attractive candidates for unsteady flow predictions in the area of propulsion system aerodynamics.

References

[1] Cousins, W.T., "History, Philosophy, Physics, and Future Direction of Aircraft Propulsion System / Inlet Integration", *Proceedings of ASME Turbo Expo 2004, Power for Land, Sea, and Air*, Vienna, Austria, 2004, pp. 305-320.

[2] Bowditch, D.N., and Coltrin, R.E., "A Survey of Inlet/Engine Distortion Compatibility," NASA TM-83421, 1983.

[3] Wellborn, S. R., Okiishi, T. H., and Reichert, B., "A study of the Compressible Flow through a Diffusing S-Duct," NASA TM-106411, 1993.

[4] Delot, A.L., Garnier, E., and Pagan, D., "Flow Control in a High-Offset Subsonic Air Intake," *47th AIAA/ASME/SAE/ASEE Joint Propulsion Conference and Exhibit*, AIAA 2011-5569, San Diego, California, 2011.

[5] Garnier, E., "Flow Control by Pulsed Jet in a Curved S-Duct: A Spectral Analysis," *AIAA Journal*, Vol. 53, No. 10, (2015), pp. 2819-2832.

[6] Delot, A.L., Berens, T.M., Tormalm, M., Saterskog, M., and Ceresola, N., "DES Computations for a Subsonic UAV Configuration with a Highly Integrated S-Shaped Inlet Duct," *52nd AIAA SciTech Aerospace Sciences Meeting*, AIAA 2014-0723, National Harbor, Maryland, 2014.

[7] Zachos, P. K., MacManus, D. G., Gil-Prieto, D., and Chiereghin, N., "Flow Distortion Measurements in Convoluted Aero Engine Intakes," *AIAA Journal*, Vol. 54, No. 9, (2016), pp. 2819-2832.

[8] Gil-Prieto, D., MacManus, D.G., Zachos, P.K., Tanguy, G., and Menzies, K., "Convoluted Intake Distortion Measurements Using Stereo Particle Image Velocimetry," *AIAA Journal*, Vol. 55, No. 6 (2017), pp. 1878-1892.

[9] Gil-Prieto, D., Zachos, P.K., MacManus, D.G., and McLelland, G., "Unsteady Characteristics of S-duct intake Flow Distortion," *Aerospace Science and Technology*, Vol. 84 (2019), pp. 938-952.

[10] Delot, A.L., and Scharnhorst, R.K., "A Comparison of Several CFD Codes with Experimental Data in a Diffusing S-Duct," *49th AIAA/ASME/SAE/ASEE Joint Propulsion Conference*, AIAA Paper 2013-3796, San Jose, California, 2013.

[11] Fiola, C., and Agarwal, R.K., "Simulation of Secondary and Separated Flow in Diffusing S-Ducts," *Journal of Propulsion and Power*, Vol. 31, No. 1, 2015, pp. 180-191.

[12] Berens, T.M., Delot, A.L., Chevalier, M., and Van Muijden, J., "Numerical Simulations for High Offset Intake Diffuser Flows," *52nd AIAA Aerospace Sciences Meeting – AIAA SciTech Forum*, AIAA Paper 2014-0371, National Harbor, Maryland, 2014.

[13] Watson, R.A., Tucker, P.G., and Menzies, K., "Unsteady Simulations of the Wellborn Diffusing S-Duct," *54th AIAA Aerospace Sciences Meeting – AIAA SciTech Forum*, AIAA Paper 2016-2126, San Diego, California, 2016.

[14] MacManus, D.G., Chiereghin, N., Gil-Prieto, D., and Zachos, P.K., "Complex Aero Engine Intake Ducts and Dynamic Distortion", *AIAA Journal*, Vol. 55, No. 7 (2017), pp. 2395-2409.

[15] Gil-Prieto, D., MacManus, D., G., Zachos, P., K., Tanguy, G., Wilson, F., and Chiereghin, N., "Delayed Detached-Eddy Simulation and Particle Image Velocimetry Investigation of S-duct Flow Distortion," *AIAA Journal*, Vol. 55, No. 6 (2017), pp. 1893-1908.

[16] Winkler, C.M., and Davis, Z., "Summary of the 3rd Propulsion Aerodynamics Workshop: S-duct Results," *53rd AIAA/SAE/ASEE Joint Propulsion Conference, AIAA Propulsion and Energy Forum*, AIAA Paper 2017-4912, Atlanta, Georgia, 2017.

[17] McMillan, M.L., Mackie, S.A., Gissen, A., Vukasinovic, B., Lakebrink, M.T., Glezer, A., Mani, M., and Mace, J.L., "Inlet Flow Control and Prediction Technologies for Embedded Propulsion Systems," NASA CR-2011-217237, 2011.

[18] Noelting, S., Gautier, S., and Wessels, M., "Simulation of an S-duct Inlet using the Lattice-Boltzmann Method," *51st AIAA/SAE/ASEE Joint Propulsion Conference, AIAA Propulsion and Energy Forum*, AIAA Paper 2015-3963, Orlando, Florida, 2015.

[19] Harloff, G., Reichert, B., and Wellborn, S., "Navier-Stokes Analysis and Experimental Data Comparison of Compressible Flow in a Diffusing S-duct," *AIAA 10th Applied Aerodynamics Conference*, AIAA Paper 92-2699-CP, Palo Alto, California, 1992.

[20] Frisch, U., Hasslacher, B., and Pomeau, Y., "Lattice-Gas Automata for the Navier–Stokes Equation," Physical Review Letters, Vol. 56, No. 14, 1986, pp. 1505–1508. DOI:10.1103/PhysRevLett.56.1505

[21] McNamara, G. R., and Zanetti, G., "Use of the Boltzmann Equation to Simulate Lattice-Gas Automata," *Physical Review Letters*, Vol. 61, Nov. 1988, pp. 2332–2335.

[22] Shan, X., and Chen, H., "A General Multiple-Relaxation-Time Boltzmann Collision Model," *International Journal of Modern Physics C*, Vol. 18, No. 4, 2007, pp. 635–643. doi:10.1142/S0129183107010887

[23] d'Humières, D., "Multiple-Relaxation-Time Lattice Boltzmann Models in Three Dimensions," *Philosophical Transactions of the Royal Society of London. Series A: Mathematical, Physical and Engineering Sciences*, Vol. 360, No. 1792, 2002, pp. 437–451.

[24] Geier, M., Greiner, A., and Korvink, J., "A Factorized Central Moment Lattice Boltzmann Method," *European Physical Journal Special Topics*, Vol. 171, No. 1, 2009, pp. 55–61. DOI:10.1140/epjst/e2009-01011-1

[25] Premnath, K. N., and Banerjee, S., "On the Three-Dimensional Central Moment Lattice Boltzmann Method," *Journal of Statistical Physics*, Vol. 143, No. 4, 2011, pp. 747–794.

[26] Ducros, F., Nicoud, F., and Poinsot, T., "Wall-Adapting Local Eddy- Viscosity Models for Simulations in Complex Geometries," Proceedings of 6th ICFD Conference on Numerical Methods for Fluid Dynamics, ICFD, Oxford, 1998, pp. 293–299.

[27] Shih, T., Povinelli, L., Liu, N., Potapczuk, M., and Lumley, J., "A Generalized Wall Function," NASA TM-113112, July 1999.

[28] Tennekes, H., and Lumley, J. L., *A First Course in Turbulence*, MIT Press, Cambridge, MA, 1972, pp. 1–103.

[29] Holman, D. M., Brionnaud, R. M., Chávez Modena, M., and Valero Sánchez., E., "Lattice Boltzmann Method Contribution to the Second High-Lift Prediction Workshop," *Journal of Aircraft*, Vol. 52, No. 4 (2015), pp. 1122-1135.

[30] Trapani, G., Brionnaud, R. M., and Holman, D. M., "XFlow Contribution to the Third High-Lift Prediction Workshop," *AIAA AVIATION Forum*, AIAA 2018-2847, Atlanta, Georgia, 2018.

[31] Brionnaud, R. M., Chávez Modena, M., Trapani, G., and Holman, D. M., "Direct Noise Computation with a Lattice-Boltzmann Method and Application to Industrial Test Cases," *22nd AIAA/CEAS Aeroacoustics Conference*, AIAA Paper 2016-2969, Lyon, France, 2016.

[32] Van Bavel, L., Holman, D. M., and García-Camprubí, M., "Dynamic Simulation of Flight Test Manoeuvres on the Diamond D-Jet," NAFEMS world congress 2013, 9-12 June, Salzburg, Austria, 2013.

[33] Hellström, L.H.O., Zlatinov, M.B., Cao, G., and Smits, A.J., "Turbulent Pipe Flow Downstream of a 90° Bend," *Journal of Fluid Mechanics*, Vol. 735, 2013, pp. 1–12. DOI: 10.1017/jfm.2013.534

[34] S-16 Turbine Engine Inlet Flow Distortion Committee, "A Methodology for Assessing Inlet Swirl Distortion", Report No. AIR5686, Society of Automotive Engineers, 2007.

[35] Gil-Prieto, D., MacManus, D.G., Zachos, P.K., and Bautista, A., "Assessment Methods for Unsteady Flow Distortion in Aero-engine Intakes," *Aerospace Science and Technology*, Vol. 72 (2018), pp. 292-304.

[36] Tanguy, G., MacManus, D.G., Garnier, E., and Martin, P.G., "Characteristics of Unsteady Total Pressure Distortion for a Complex Aero-engine Intake Duct," *Aerospace Science and Technology*, Vol. 78 (2018), pp. 297-311.

2019-08-16

Unsteady swirl distortion characteristics for S-ducts using Lattice Boltzmann and time-resolved, stereo PIV methods

Guerrero-Hurtado, Manuel

AIAA

Guerrero-Hurtado M, Zachos PK, MacManus DG, et al., (2019) Unsteady swirl distortion characteristics for S-ducts using Lattice Boltzmann and time-resolved, stereo PIV methods. In: AIAA Propulsion and Energy 2019 Forum, 19-22 August 2019, Indianapolis, IN, USA

https://doi.org/10.2514/6.2019-4275